Biofabrication

International Society for Biofabrication

PAPER • OPEN ACCESS

Internally crosslinked alginate-based bioinks for the fabrication of *in vitro* hepatic tissue models

To cite this article: Giuseppe Guagliano *et al* 2023 *Biofabrication* **15** 035018

IOP Publishing *Biofabrication* **15** (2023) 035018 https://doi.org/10.1088/1758-5090/acd872

Biofabrication

OPEN ACCESS

RECEIVED
13 February 2023

REVISED
5 May 2023

ACCEPTED FOR PUBLICATION
24 May 2023

PUBLISHED
1 June 2023

PAPER

Internally crosslinked alginate-based bioinks for the fabrication of *in vitro* hepatic tissue models

Giuseppe Guagliano[1], **Cristina Volpini**[2,3], **Jacopo Camilletti**[1], **Francesca Donnaloja**[1],
Francesco Briatico-Vangosa[1], **Livia Visai**[2,3,4,6] **and Paola Petrini**[1,5,6,*]

[1] Department of Chemistry, Materials, and Chemical Engineering 'G. Natta', Politecnico di Milano, Milan, Italy
[2] Molecular Medicine Department (DMM), Center for Health Technologies (CHT), UdR INSTM, University of Pavia, Pavia, Italy
[3] Medicina Clinica-Specialistica, UOR5 Laboratorio Di Nanotecnologie, ICS Maugeri, IRCCS, Pavia, Via Boezio, 28-27100 Pavia, Italy
[4] Interuniversity Center for the Promotion of the 3Rs Principles in Teaching and Research (Centro 3R), Università di Pavia Unit, Pavia, Italy
[5] Interuniversity Center for the Promotion of the 3Rs Principles in Teaching and Research (Centro 3R), Politecnico di Milano Unit, Milan, Italy
[6] These authors contributed equally.
[*] Author to whom any correspondence should be addressed.

E-mail: **paola.petrini@polimi.it**

Keywords: biofabrication, extracellular matrix, extrusion bioprinting, HepG2, liver model

Supplementary material for this article is available online

Abstract

Bioprinting is a key technique to fabricate cell-laden volumetric constructs with controlled geometry. It can be used not only to replicate the architecture of a target organ but also to produce shapes that allow for the mimicry, *in vitro,* of specific desired features. Among the various materials suitable to be processed with this technique, sodium alginate is currently considered one of the most appealing because of its versatility. To date, the most widespread strategies to print alginate-based bioinks exploit external gelation as a primary process, by directly extruding the hydrogel-precursor solution into a crosslinking bath or within a sacrificial crosslinking hydrogel, where the gelation takes place. In this work, we describe the print optimization and the processing of Hep3Gel: an internally crosslinked alginate and ECM-based bioink for the production of volumetric hepatic tissue models. We adopted an unconventional strategy, by moving from the reproduction of the geometry and the architecture of liver tissue to the use of bioprinting to fabricate structures that can promote a high degree of oxygenation, as is the case with hepatic tissue. To this end, the design of structures was optimized by employing computational methods. The printability of the bioink was then studied and optimized through a combination of different *a priori* and *a posteriori* analyses. We produced 14-layered constructs, thus highlighting the possibility to exploit internal gelation alone to directly print self-standing structures with finely controlled viscoelastic properties. Constructs loaded with HepG2 cells were successfully printed and cultured in static conditions for up to 12 d, underlining the suitability of Hep3Gel to support mid/long-term cultures.

1. Introduction

Extrusion-based 3D-bioprinting (EBB) is rapidly emerging as a potent application of additive manufacturing processes in the field of life sciences. The ability to rapidly fabricate highly reproducible cell-laden constructs, characterized by controlled geometry and porosity, is progressively being understood as a key opportunity both for regenerative medicine applications and for the production of complex *in vitro* models [1–4].

Additionally, the shape is not the only parameter that can be customized and tailored when exploiting EBB approaches. One of the most interesting aspects related to this fabrication technique is directly linked to the wide choice of materials (usually in the form of hydrogels)—and combination of them—that can be exploited to tailor application-based bioinks, thus enabling a complete control over the fate and behaviour of cultured cells through time [5–8]. Among them, sodium alginate currently represents an extremely popular candidate [9, 10]. This natural polysaccharide is extracted from brown algae, is highly soluble in water, and, due to the negative charges on its macromolecular chains, can be chemically crosslinked through the exposure to divalent cations (usually Ca^{2+} ions) [11]. Alginate hydrogels can also be produced both by external and internal gelation and their viscoelastic properties can be tuned by directly acting on the formulation [12]. These aspects, together with the ability of alginate hydrogels to support the growth of embedded cells, have contributed to their recognition as flagship materials for biofabrication approaches [13, 14].

When processed with EBB, alginate-based bioinks are usually crosslinked by external gelation. To this end, the hydrogel precursor solution is extruded within a crosslinking bath, or within a sacrificial supporting hydrogel, where Ca^{2+} are dissolved and as such being immediately available. This causes the instantaneous transition from 'sol' to 'gel' phase [15–18]. Conversely, in the field of bioprinting, internal gelation has only been proposed as a pre-crosslinking strategy intended to improve the printability of alginate-based inks [19]. Internal, as opposed to external, gelation relies on triggering the progressive release of the Ca^{2+} ions that are already homogeneously dispersed throughout the hydrogel precursor, not being directly available, thus achieving the gelation [20]. One of the most common strategies to produce alginate hydrogels with this technique involves suspending $CaCO_3$ within the hydrogel precursor and then dissolving it by lowering the pH, thus enabling the progressive release of Ca^{2+} ions [12]. As a result, the internal gelation process allows to fully control the crosslinking kinetics of the hydrogel, as these kinetics are themselves directly related to the speed at which the divalent cations are released. This property makes internally crosslinked alginate hydrogels particularly appealing for biofabrication as it allows to tailor the rate at which the final viscoelastic properties are reached, thus functioning as dynamic materials that are potentially suitable for reactive bioprinting approaches [21]. Additionally, with internal gelation, the crosslinking ions are released throughout the volume of the hydrogel precursor and, as a consequence, these hydrogels are characterized by a homogeneous degree of gelation throughout their structure. This avoids the uncontrolled formation of crosslinking gradients or core–shell structures which are typical of externally crosslinked hydrogels [20, 22, 23]. In this sense, the possibility to exert complete control over the viscoelastic properties of internally crosslinked alginate hydrogels makes them particularly interesting for applications in which constructs need to replicate a mechanical environment, as in the fabrication of *in vitro* models [24].

Aiming to fabricate macroporous cell-laden constructs we propose, in this paper, a systematic and lean methodology which is designed to optimize the printability of Hep3Gel, and which considers the possibility of reactively bioprinting it. Starting from the choice and the design of the to-be-printed geometry, the described methodology is partitioned into three different phases which are linked in a feed-forward chain. The first constitutes an *a priori* study of printability. Evidence obtained at this stage is the starting point for the subsequent phase, during which simple planar geometries are printed, implementing different combinations of parameters. The most promising combinations then enter the last phase which includes the printing of the full geometry, allowing to refine the remaining parameters and to determine the optimal printing configuration. The tuned printing set-up is then implemented to produce cellularized constructs to be cultured in static conditions.

2. Experimental section

2.1. Materials

Alginic acid sodium salt, D-(+)-glucono-delta-lactone (GDL), calcium carbonate, calcium chloride, and Alamar blue were acquired from Sigma-Aldrich (US). E-MEM with Earl's salt, fetal bovine serum, sodium pyruvate, and penicillin–streptomycin were acquired from Euroclone (IT). Trypan blue was acquired from Gibco (US), and Live/Dead kit was acquired from Invitrogen (US). HepG2 cells at passage 22 were kindly provided by Istituto Zooprofilattico Sperimentale della Lombardia ed Emilia Romagna 'B. Ubertini'.

2.2. Methods

2.2.1. Design of the geometry and oxygen diffusion

Two major requirements were considered when designing the geometry of the constructs. First, the dimensions of the constructs should have facilitated their printing and culturing directly within a 12-well plate. Given these, a cylindrical geometry measuring 10 mm in diameter and 3 mm in height was designed with Inventor® (Autodesk, US). Then, the geometry of the scaffold should have promoted the homogeneous exchange of oxygen and nutrients throughout the volume of the construct, even in its inner regions. Additionally, aiming not to overstress cultured cells, the threshold to reach the oxygen equilibrium was set equal to 30 min. Aiming to *a priori* validate the designed geometry, we ran multiphysics computational simulations (computational fluid dynamics and mass transport analysis) with the COMSOL Multiphysics® software (COMSOL Inc., US). Simulations relied on the '*Transport of a Diluted Species*' physics module in the transitory state (0, 10, 30 min). Mass transport equations (equations (1)

Table 1. Parameters implemented for the computational simulation of the oxygen distribution [25].

Parameter	Value
Oxygen diffusion coefficient in the medium	2×10^{-9} [$\mathrm{m^2\,s^{-1}}$]
Oxygen diffusion coefficient in the construct	2×10^{-9} [$\frac{m^2}{s}$]
C_0 in the medium	0.195 [$\mathrm{mol\,m^{-3}}$]
Density of culture medium at 37 °C	1000 [$\mathrm{Kg\,m^{-3}}$]

and (2)) were implemented in the model together with the parameters listed in table 1

$$\frac{\partial c_i}{\partial t} + \nabla \cdot J_i = R_i \tag{1}$$

$$J_i = -D_i \nabla \mathrm{c}_i \tag{2}$$

where J_i is the oxygen flux, the reaction term was set to null ($R_i = 0$) in the control volume and D_i is the oxygen diffusion coefficient in the medium. As boundary conditions, the initial oxygen concentration C_0 in the medium was set as shown in table 1, and null oxygen concentration was set in the construct.

2.2.2. Preparation of the bioinks

Hep3Gel was produced through alginate internal crosslinking, as previously described [20]. Then, immediately after the addition and mixing of GDL, samples were loaded into 3 ml pneumatic bioprinting cartridges (CELLINK, SE), capped with a 0.22 μm luer-lock syringe filter (Primo Filters, Euroclone, IT), and incubated until needed at 37 °C, 95% humidity, 5% CO_2.

Two other hydrogels, the first one made with alginate only (ALG), and the second one made of a blend of alginate and gelatin (GEL), were produced as previously described, processed in the same way as Hep3Gel, and used as controls [20]. All the hydrogels described in this study were produced through alginate internal gelation, a detailed insight on the process to produce them is illustrated in figure S1.

2.2.3. Time-dependent rheological characterization

Beginning with an awareness of the crosslinking kinetics of the materials under consideration, their viscoelastic properties were characterized during the crosslinking process at different time-points, from the beginning of the reaction onwards (3 h, 4 h, and 5 h) with frequency-sweep tests performed with a modular rheometer (MCR502e, Anton-Paar, AT) equipped with a 25 mm parallel plate geometry (Serial number: 52890, Anton-Paar, AT). After having assessed that no slippage was occurring between the plates, analyses were performed in the frequency range 0.1–20 Hz, with a 0.5 mm gap between plates, and imposing a constant 0.5% shear-strain amplitude, well within the linear range. The temperature was set at 37 °C and controlled with a Peltier's plate and hood system. The final viscoelastic properties of the Hep3Gel and control materials at the end of crosslinking (24 h after the beginning of the reaction) has been previously reported [20].

The crosslinking kinetics of the hydrogels were characterized by measuring the moduli G' and G'' at different time points from the beginning of gelation, including the end of crosslinking (0–1–2–24 h). Measurements were performed at the constant frequency of 1 Hz, applying a 0.5% shear strain. These tests were carried out both at 24 °C and 37 °C to investigate the possible impact of temperature on the kinetics or on the final viscoelastic properties of materials.

2.2.4. Microstructural characterization of bioinks

The frequency-dependent response of the viscoelastic properties of each hydrogel was interpreted by applying the generalized Maxwell's model (GMM) at different time-points from the beginning of crosslinking (3 h, 4 h, 5 h, and 24 h), allowing us to understand the microstructural evolution of the hydrogels during gelation. The microstructure was reported in terms of the mesh size, ξ. This parameter gives an estimation of the distance between two adjacent crosslinking sites on the same macromolecular chain.

The frequency-sweep analyses carried out in the linear viscoelastic regime can be interpreted through the GMM, which consists of n Maxwell's elements linked in parallel. Each element is composed of one spring (elastic component) connected in a series to one dashpot (viscous component). These two components are characterized by a specific modulus G_i, and viscosity η_i, respectively. As already reported, the relaxation times $\lambda_i = G_i/\eta_i$, of each Maxwell element were progressively scaled by a factor of 10 (e.g. $\lambda_i = 10{\cdot}\lambda_{i+1}$) and a pure elastic element (with relaxation time G_e) was linked in parallel with the other Maxwell's elements [26–29].

By applying this model, the dependence of G' and G'' from the frequency can be predicted with equations (3) and (4)

$$G' = G_e + \sum_{i=1}^{n} G_i \frac{(\omega\lambda_i)^2}{1 + (\omega\lambda_i)^2} \tag{3}$$

$$G'' = \sum_{i=1}^{n} G_i \frac{(\omega\lambda_i)^2}{1 + (\omega\lambda_i)^2} \tag{4}$$

where ω is the angular frequency, and λ_i and η_i are the relaxation time and viscosity associated with the ith Maxwell's element, respectively. It is important to underline that it was possible to apply these equations because all the materials had already crossed the gel-point at the considered time-points ($G' > G''$). If this condition is not satisfied the GMM cannot be applied since a crosslinking network would not yet have formed.

The microstructure of the inks was then estimated by exploiting the model to fit data from the frequency-sweep tests. It was found the number of Maxwell's elements minimizing the error between the theoretical results and experimental data (equation (5))

$$\text{Error} = (n+2)\cdot\chi^2 \tag{5}$$

where χ^2 is the Chi-squared error, n is the number of Maxwell elements, which varies from 1 to 10, and $n + 2$ is the number of parameters describing the GMM.

G_e and G_i, obtained by the fitting (equations (1) and (2)), were combined to compute the fully relaxed shear modulus (G_∞), as in equation (6)

$$G_\infty = G_e + \sum_i^n G_i \tag{6}$$

where n is the number of Maxwell's elements minimizing the error and fitting the frequency curves. G_∞ can be then related to the microstructure of the materials by exploiting the theory of rubber elasticity, as in equation (7)

$$\xi = \sqrt[3]{\frac{6RT}{\pi N_\text{A} G_\infty}} \tag{7}$$

where R is the universal gas constant, T is the absolute temperature, N_A is the Avogadro constant and ξ is the estimated mesh size. All these computations were carried out in MATLAB R2022a (MathWorks, US).

2.2.5. Time-dependent a priori assessment of printability

Two different rheological analyses were performed with the same geometry, gap and temperature levels that were used for the tests described in section 2.2.3.

To be tested, samples were retrieved from the cartridges 3 h, 4 h, and 5 h after the beginning of the crosslinking process and loaded on the rheometer plate. In this way, samples were analysed during crosslinking. Homologous tests on samples at the end of crosslinking (24 h after the beginning of the reaction) were previously carried out [20].

The first test (yielding test) was performed by imposing a shear-stress amplitude sweep, in the 0.1–100 Pa range, carried out at the constant frequency of 1 Hz, with a 0.5% shear-strain amplitude. The second test (recovery test) was divided into three different experimental steps, with samples firstly undergoing a constant 0.5% shear-strain amplitude, at the constant frequency of 1 Hz for 2 min; samples were then tested for a further 2 min with a 100% shear-strain amplitude at the constant frequency of 1 Hz; finally, a 0.5% shear strain stimulation was carried out for 3 min at the constant frequency of 1 Hz.

2.2.6. 3D-printing of mono- and bi-layered geometries

Cartridges were loaded into controlled temperature pneumatic printheads (Standard 3 ml pneumatic printhead, serial number: 01348, CELLINK, SE), and mounted on a pneumatic bioprinter (BIO X, serial number: 181428 CELLINK, SE). Unless stated otherwise, the printhead temperature was always set at equal to 37 °C. In principle, all tests were performed with a 12.7 mm long 22 G nozzle (CELLINK, SE) 3 h, 4 h, 5 h, and 24 h from the beginning of crosslinking.

Firstly, the pressure was varied until the minimum pressure (M_P) required to vertically extrude a continuous filament of Hep3Gel was identified. 2 cm long fibres were then printed on a glass coverslip with the printhead moving at 5, 6, 7, 8, and 9 mm s^{-1}, and adopting for each speed both M_P and $M_P + 5$ kPa. The Fibres were then observed with an optical microscope (BH-2, Olympus, JP) and their diameter was measured with FIJI in 15 different random points [30]. These measurements were used to compute the uniformity coefficients (U), as in equation (8)

$$U = \frac{L_\text{real}}{L_\text{ideal}} \tag{8}$$

where L_ideal is the ideal diameter of a straight and homogeneous fibre, coinciding with the internal diameter of the nozzle (0.410 μm for the 22 G, and 0.250 μm for the 25 G).

Planar cross-sections of the full geometry validated from section 2.2.1 were then printed with the same printing parameters that were used to print fibres. In particular, 1 cm in diameter, bi-layered circular grids were printed with a 10% infill density, adopting a grid infill pattern. These geometries were then photographed from above with a high-resolution camera (iPhone 12 Pro Max, Apple Inc., CA, US) and with a transmitted light optical microscope, with a 4X magnification. Perimeters and pores were then measured (with FIJI) to compute the perimeter coefficient (P_e) and the pore coefficient (P_r), according to equations (9) and (10), respectively

$$P_e = \frac{1}{\left[\left|\frac{1}{2}\times\left(\frac{L_{bR}}{L_{0R}}+\frac{L_{bL}}{L_{0L}}\right)-1\right|+1\right]\times\left[1+\frac{1}{2}\times\left(\frac{\text{SD}_{bR}}{L_{0R}}+\frac{\text{SD}_{bL}}{L_{0L}}\right)\right]} \tag{9}$$

where L_{0x} and L_{0y} are the theoretical lengths of the horizontal and vertical sides. L_{bx} and L_{by} are the average lengths of the horizontal and vertical printed sides and SD_{bx} and SD_{by} are their standard deviations

$$P_r = 0.77\frac{(\text{Pore Perimeter})^2}{4\pi\times(\text{Pore Area})} \tag{10}$$

where 0.77 is a shape-dependent coefficient determined as shown in supplementary materials, coherently and with a previously determined formula [31].

These data were then combined, as shown in equation (11), to calculate the printability coefficient (P) aiming to quantify the printability of hydrogels

$$P = \frac{3}{\frac{1}{U}+\frac{1}{P_c}+\frac{1}{P_t}}. \tag{11}$$

This same multi-parametric analysis was then carried out with 12.7 mm long 25 G cylindrical needles and 32 mm long 25 G conical nozzles (CELLINK, SE), but only on samples that had been crosslinked for 24 h.

2.2.7. 3D-bioprinting of full-sized constructs

From the analyses of coefficients described in section 2.2.5, it was possible to identify the most effective combinations of time-point (i.e. time from the beginning of crosslinking), extrusion pressure, printhead speed, and type of needle required. These combinations of parameters were adopted to print the fully designed geometry, and the focus was put on adjusting printing parameters in order to avoid a structural collapse during the printing process. To this end, pre-flow time, heights of layers, and infill density were adjusted until reaching the structural integrity of the printed construct. At this stage, we determined the optimal combination of printing parameters.

2.2.8. Resolution of the optimized process

Once the printing process was optimized for each of the examined bioinks, the resolutions—the minimum distance at which two contiguous fibres can be printed without merging—were analysed by printing a serpentine with a decreasing curvature radius (5 mm, 2 mm, 1 mm, 0.7 mm, 0.5 mm, and 0.4 mm), and measuring the distance between adjacent fibres with FIJI.

2.2.9. Viscoelastic properties of printed constructs

The viscoelastic properties of constructs produced with Hep3Gel, GEL and ALG were measured at different time-points after printing (0 min, 15 min, 30 min, 45 min, and 60 min). 25 mm × 0.7 mm cylindrical constructs with a 100% infill density were directly printed into disposable rheometer dishes (EMS/CTD 600, Anton-Paar, Cat. #4847, AT), with the optimal printing parameters determined as described in section 2.2.6. Samples were tested at 37 °C with the rheometer mounting the 25 mm plate-plate geometry by the means of frequency-sweep tests, in the 0.1–20 Hz frequency range, with a constant 0.5% shear-strain and a 0.5 mm gap between plates.

2.2.10. Post-processing of Hep3Gel and control materials

The possibility to cure printed constructs immediately after their printing was also explored. To this end, solid cylindrical samples measuring 25 mm in diameter and 0.7 mm in height were printed with each ink, by adopting the full set of optimized printing parameters, as determined in section 2.2.7. The adoption of solid geometries for carrying out these analyses was mandatory, since the macropores that characterize the shape designed for cell-laden constructs might lead to the formation of gaps between the plates of the rheometer, thus impairing the measurements. These samples were treated with 0.1%, 0.5%, and 1% (w/v) solutions of $\mathrm{CaCl_2}$ in complete HepG2 medium. After 30 s the $\mathrm{CaCl_2}$ solution was removed, samples were rinsed with fresh medium and finally tested through frequency-sweep analyses in the frequency range 0.1–20 Hz, imposing a constant shear-strain of 0.5%. For these tests temperature was set equal to 37 °C, and controlled with a Peltier's plate and hood system.

2.2.11. Cell culture and embedding

HepG2 cells were kindly provided by the 'Istituto Zooprofilattico Sperimentale della Lombardia e dell' Emilia-Romagna'. Cells were cultured and expanded in HepG2 complete medium, composed of E-MEM with Earl's salts, 10% (v/v) fetal bovine serum (FBS), 1% (v/v) Na-pyruvate, 1% (v/v) Glutamine, and 1% (v/v) penicillin-streptomycin (Lonza, Lot. #2MB027, BE). During the whole expansion process, the medium was refreshed every 48 h. After a suitable number of cells was reached, they were detached with trypsin (Lonza, Lot. #4MB146, BE), and embedded before crosslinking within pre-hydrogel solutions at the final concentration of 3×10^6 cells $\mathrm{ml^{-1}}$, as previously described [20].

2.2.12. Viability analyses and static culture

Cellular viability was measured at different stages. HepG2-loaded Hep3Gel, GEL and ALG were used to print full-sized constructs, according to the optimal printing parameters given in section 2.2.6. Immediately after printing, the constructs were cured for 30 s with a 0.1% (w/v) $\mathrm{CaCl_2}$ solution in a complete HepG2 medium. They were then rinsed with, and then immersed in fresh medium and finally incubated at 37 °C, 95% humidity, and 5% $\mathrm{CO_2}$. Cell viability was then quantitatively evaluated with an Alamar blue assay 4 h after the printing and after 3, 6, 9, and 12 d in culture. Quantitative measurements of the viability were carried out by incubating the constructs for 24 h in a 10% (v/v) solution of Alamar blue in EMEM medium. After 24 h incubation results were obtained by reading the $OD_{600\text{-}690}$ with a spectrophotometer (ClarioStar, BMG Labtech, DE) [32]. During this experiment, the medium was refreshed every 24 h. Quantitative viability results were obtained by normalizing the obtained data as a percentage of the values after 4 h.

Qualitative viability measurements were performed immediately after the printing and on the 15th day in culture via confocal laser scanning microscope (CLSM) (SP8, Leica, DE) fluorescence observations with a 20X magnification. To this end, scaffolds were stained with a Live/Dead kit (Invitrogen, US) according to the producer's protocols. Images were acquired exploiting the Leica proprietary navigator tool, aiming to provide a more general view of the samples.

2.2.13. Statistical analyses

All experiments were carried out at least in technical duplicate and on at least two independent batches. Data are expressed as mean ± standard deviation (SD). SDs are reported as bars or as ranges, depending on the graph type; where not visible, error bars are graphically smaller than plotted symbols. Normality tests were performed to assess the Gaussian distribution of data and *t*-tests, or Mann–Whitney tests were used to compare two groups of data, depending on their being normally distributed or not. Two-way ANOVA with Bonferroni correction was used to run multiple comparisons. Data representation and statistical analyses were carried out with GraphPad Prism (GraphPad Software, Inc., CA, US), release 9.0.2. Different degrees of significance were considered (ns $p > 0.05$, $^{*}\ p < 0.05$, $^{**}\ p < 0.01$, $^{***}\ p < 0.001$, $^{****}\ p < 0.0001$).

3. Results

3.1. 3D-bioprinting to enhance oxygen diffusion

Numerical simulations were performed to assess the degree of oxygenation that can be reached by statically culturing constructs which are characterized by the designed geometry. These results were compared to those obtainable by statically culturing constructs characterized by null porosity levels throughout their structure (figure 1).

During these simulations the equilibrium was reached after 30 min. Data related to the time-dependent oxygenation profile during the transitory phase (from time = 0 min to time = 30 min) are reported in supplementary materials (figure S2). This analysis shows significant differences between the two geometries and highlights that the adoption of a macroporous structure facilitates the oxygenation of the constructs. Conversely, the non-porous scaffolds were characterized by a decreasing gradient of oxygenation from the peripheral regions to the centre. Quantitatively, once the equilibrium is reached, the macroporous geometries are up to 3–4 times more oxygenated than the non-porous geometries. The successful establishment of a homogeneous degree of oxygenation within 30 min, with the values of O_2 concentration in the printed constructs being the same as in fresh medium, validates the designed geometry. In light of this, the printing of the engineered bioinks will be optimized around this specific shape.

3.2. Time-dependent viscoelastic properties and microstructures of the bioinks

The time-dependent viscoelastic properties of Hep3Gel and control materials were measured in terms of conservative modulus (G) and loss modulus (G''). This was done during the crosslinking of hydrogels, at different time-points from the beginning of gelation (figures 2(a)–(c)).

Results from these frequency-sweep tests show that, at the examined time-points, Hep3Gel, GEL and ALG samples have already crossed the gel-point, being their conservative modulus G' greater than their loss modulus G''. It was also possible to observe variations in viscoelastic properties. It is notable that G' increased through time whereas almost no variations were recorded for the loss modulus G''. This behaviour is also highlighted by the progressive decrease of the loss factor tanδ in each of the samples that were examined (figure 2(d)). The data obtained by applying the GMM clearly indicate that mesh size (i.e. the average distance between two contiguous crosslinking sites) decreased over time (figure 2(e)). This trend was barely noticeable for the GEL and ALG samples but was considerably more evident in the Hep3Gel results.

This behaviour is consistent with the overall trend of the viscoelastic properties of Hep3Gel, GEL, and ALG as a function of time. From figure S3 it is clear that the GEL and ALG share extremely similar crosslinking kinetics, reaching the gel-point after about 1 h from the beginning of the crosslinking. Differently, in the case of Hep3Gel the progression of the gelation is delayed, and the transition from 'sol' to 'gel-phase' is reached after roughly 2 h from the beginning of the reaction. However, this recorded delay does not affect the final properties of Hep3Gel, that are comparable to those recorded for the controls.

Additionally, no significant differences were recorded between measurements of G' and G'' at 24 and 37 °C. This fact does not only indicate that in the considered temperature range the viscoelastic behaviour of hydrogels is independent from temperature, but also indicates that—at the concentration adopted

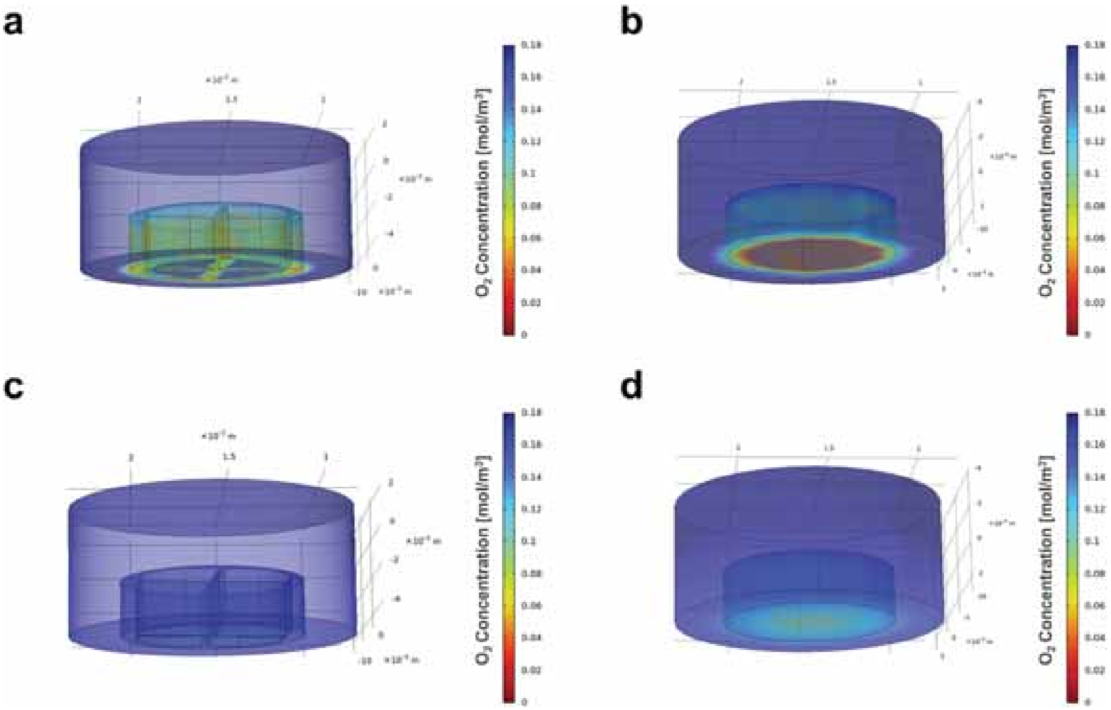

Figure 1. Numerical simulations of the oxygen diffusion through the constructs. (a) (b) The oxygen distribution at time-point 0 min in the macroporous construct and in the homogeneous one, respectively. (c) (d) The oxygen distribution after 30 min in the macroporous construct and in the homogeneous one, respectively.

to produce GEL—gelatin is not contributing to the structure of the crosslinking mesh. Generic secondary interactions would be affected by the temperature changes. The independency from temperature of the viscoelastic properties of all the materials indicates a successful stable crosslinking, within the temperature range of interest for producing hydrogels and culturing cells.

3.3. Optimization of the printing parameters

3.3.1. A priori assessment of the printability

Data from the shear stress amplitude sweep (yielding test) highlight that at each time-point, and for all the materials, there is a determined shear stress amplitude at which G'' starts prevailing over G'. This indicates that under such stresses the material begins to behave like a fluid rather than as a solid (figures 3(a)–(c)).

The recovery test (figures 3(d)–(f)) on the other hand indicated that, at each of the examined time-points, Hep3Gel and control materials can recover their original viscoelastic properties more-or-less progressively, after having undergone a high-strain deformation.

3.4. Optimization of the printing parameters as a function of the crosslinking kinetics

The minimum extrusion pressure, defined as the minimum pressure at which a filament of bioink can be extruded continuously (figure 4(a)) was determined for each material, and at each time-point of interest. These values are characterized by a similar time-dependent trend for both the Hep3Gel and control materials. However, while GEL and ALG display comparable values, especially after 4, 5, and 24 h from the beginning of crosslinking, Hep3Gel is characterized by lower minimum extrusion pressures in the early steps, that become progressively more similar to the ones of control bioinks (figure 4(b)).

The multiparametric analysis of the shape-fidelity results revealed that, for the examined application, the printability coefficient P comes progressively closer to 1 (that is the optimal value for this parameter). The difference from the unit value is minimized after 24 h from the beginning of crosslinking (figure 4(c)). The detailed results obtained at each of the considered time-points for the uniformity coefficient U, the perimeter coefficient P_e, and the pore coefficient P_r are reported in supplementary materials (figures S4–S7). Macroscopic observations of the printed geometries (figures 4(d)–(f)) indicate the qualitative correlation between values of printability and the quality of the printed geometries and highlight the impact of this parameter on printing quality.

Based on these results, we were able to conclude that the optimal time-point to print the examined bioinks was 24 h from the beginning of the crosslinking. Additionally, it was possible to identify for each material the most promising combination of printhead speed and extrusion pressure. In this context,

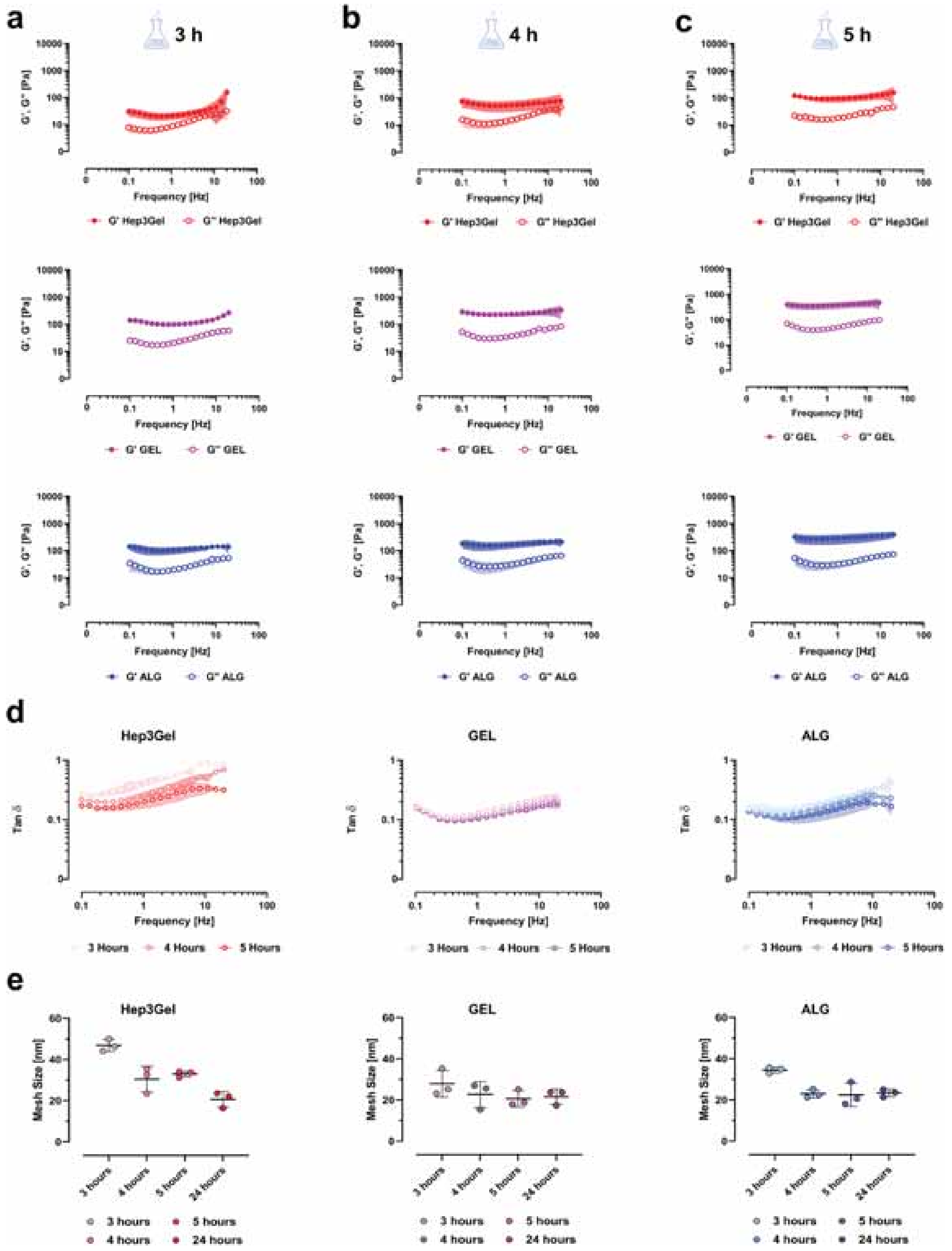

Figure 2. Time-dependent viscoelastic properties of Hep3Gel and control materials. Viscoelastic properties in terms of conservative (G′) and loss modulus (G′′) of the engineered hydrogels, measured through frequency-sweep tests after (a) 3 h, (b) 4 h, and (c) 5 h from the beginning of crosslinking. (d) The loss factor tanδ decreases through time for each of the materials considered. (e) The size of the crosslinking meshes of Hep3Gel, GEL, and ALG, computed by interpreting the rheological parameters of the bioinks with the generalized Maxwell's model. The rheological behaviour of the materials, as well as their microstructural features, were characterized as a function of time, at different time-points (3, 4, and 5 h) from the beginning of crosslinking, while the gelation was still underway.

it was observed that, for each bioink, the best results were obtained when the printing was carried out at the minimum extrusion pressure.

It was, however, impossible to fabricate the fully sized constructs with the determined printing parameters since the structures tended to collapse between 50% and 65% of the fabrication process progression. This issue was overcome by switching from the 22 G nozzle to a 25 G one, both in a cylindrical and conical configuration.

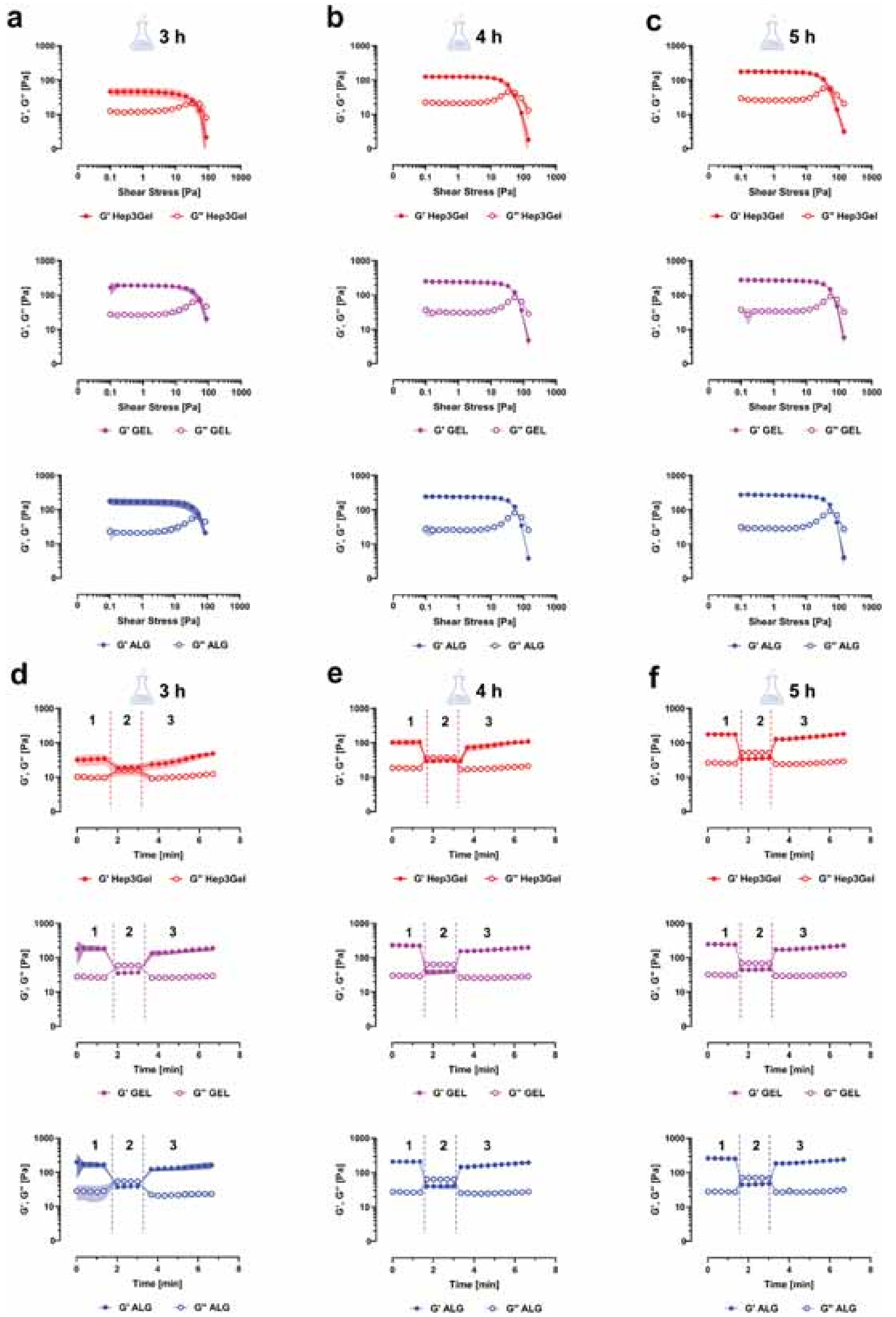

Figure 3. A priori evaluation of the printability through rheological analyses. Results of the yielding test indicates that all materials display a flow-point from which G′′ prevails over G′ at (a) 3 h, (b) 4 h, and (c) 5 h from the beginning of crosslinking. Recovery test highlights that after (d) 3 h, (e) 4 h, and (f) 5 h from the beginning of crosslinking, all the hydrogels can—progressively—recover their original viscoelastic properties after a high strain solicitation. On each plot experimental intervals 1, 2, and 3 are highlighted; they were designed to mimic the inks in the cartridge before the printing, the ink during the extrusion process, and the ink at the steady-state after the extrusion, respectively.

According to the data obtained when printing with the 22 G needle, the shape-fidelity was thus characterized after 24 h from the beginning of crosslinking, using for each material the previously determined optimal printhead-speed, in combination with the minimal extrusion pressure.

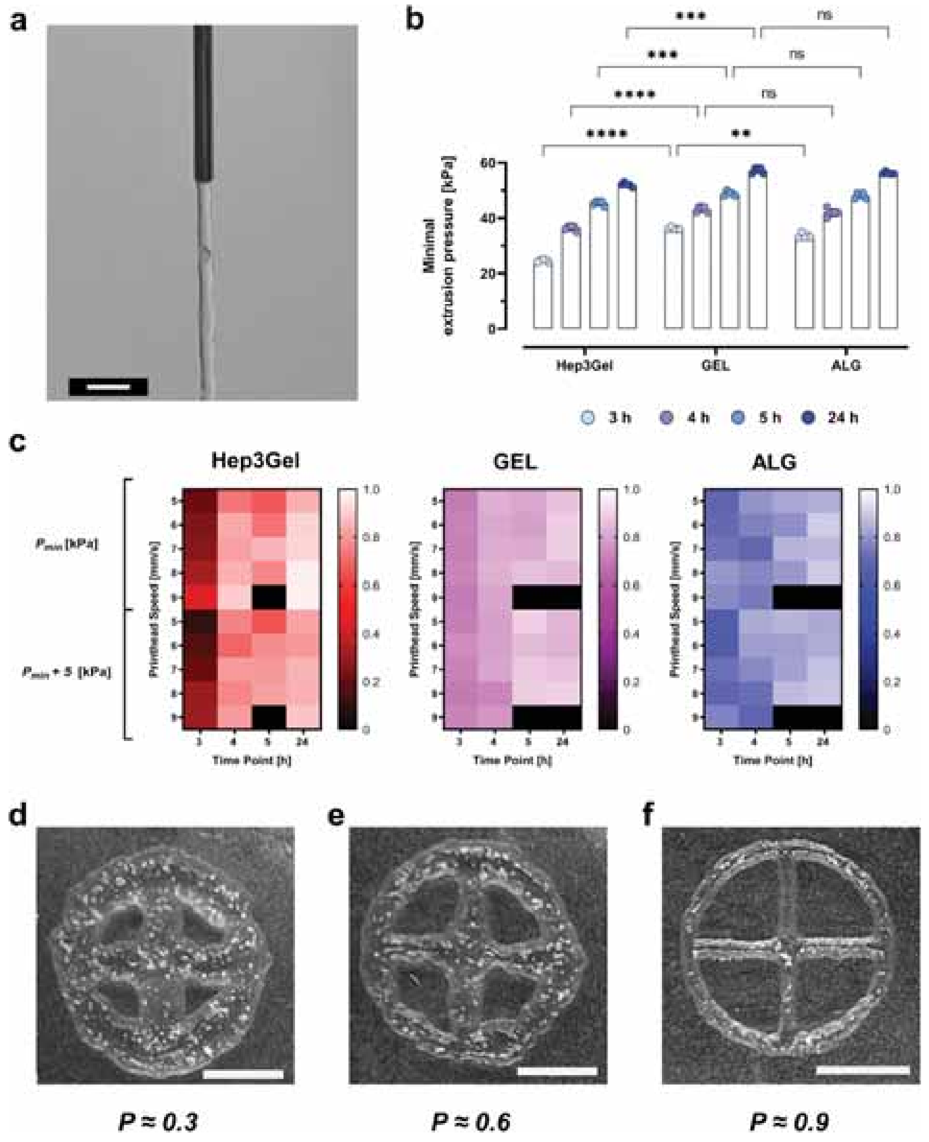

Figure 4. Printability analyses with a 22 G cylindrical needle. (a) The extrusion of a continuous and straight filament is obtained by implementing the minimal extrusion pressure. Specifically, the image refers to a sample produced with Hep3Gel; the scale-bar corresponds to 2 mm. (b) Minimal extrusion pressures (P_{min}) measured at the examined time-points for each material. (c) Heatmaps reporting the values of the printability coefficients (P) for each material, in different combinations of extrusion pressure and printhead speed, at different time-points. Black squares indicate a condition in which the material could not be printed due to fibre fragmentation, or to the occlusion of pores. Qualitative outcomes of the printing process with printability ≈0.3 (d), printability ≈0.6 (e), and printability ≈0.9. Each picture refers to a sample fabricated with Hep3Gel, and all the scale-bars correspond to 5.0 mm.

These data show consistent differences in terms of minimum extrusion pressure with a cylindrical and a conical needle (table 2). Despite this divergence, it was possible to obtain, for each bioink and with both set-ups, values close to the unit for each of the computed shape-fidelity coefficients, without any statistically significative differences between the cylindrical and the conical nozzles (figure 5).

In these conditions, the finer tuning of the printing parameters was achieved through a trial-and-error approach, leading to the final printing parameters reported in table 2.

The full set of optimized parameters was then used to quantify the resolution of the process that can be reached with Hep3Gel and control materials. Significative differences were revealed between the cylindrical and the conical nozzle, with the cylindrical one allowing to consistently reach lower values (figure 6(a)). This difference, however, did not influence the printing of the whole 14-layered constructs. These were produced without structural issues and without macroscopic defects, at a level which would impair the designed macroporous structure, with both the cylindrical and the conical extrusion configuration (figures 6(b) and (c)).

3.5. Snap-stabilization of the printed constructs through external gelation

Rheological analyses were carried out on cylindrical printed constructs to understand if, and how, the

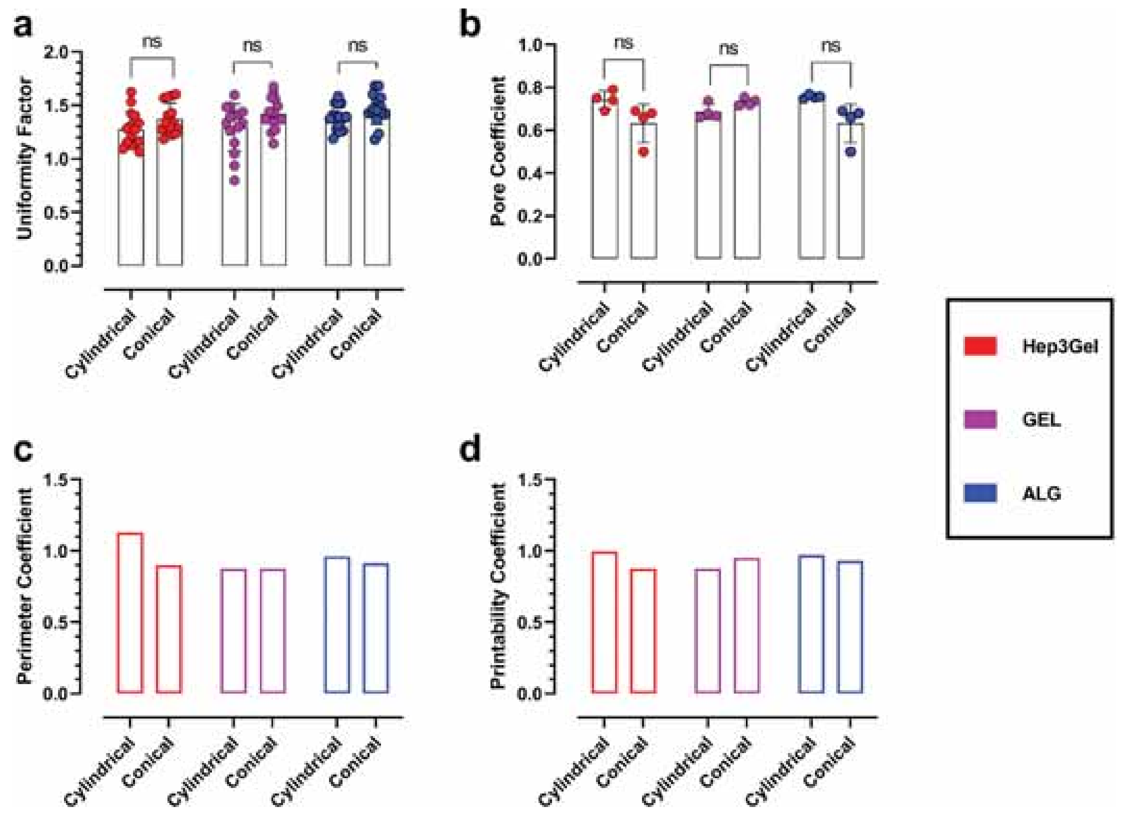

Figure 5. Multiparametric analysis of the printability with a 25 G nozzle. The picture reports the values of the (a) uniformity factor (U), (b) pore coefficient (P_r), (c) perimeter coefficient (P_e), (d) and their combination into the printability coefficient (P). Coefficients were measured on geometries printed both with a cylindrical and with a conical nozzle after 24 h from the beginning of crosslinking, by implementing for each material its minimal extrusion pressure, and the optimal printhead speed determined in figure 4 No statistical analyses are reported in panel (c) and (d) since the calculation of these coefficient already considers the mean and standard deviations of different measurements and provides a single value as output.

Table 2. Summarization of the optimized printing parameters for Hep3Gel and control materials.

	Parameter							
	Nozzle	Time-point	Pressure	Printhead speed	First layer height	Pre-flow delay	Post-flow delay	Infill density
Hep3Gel	Conical (25 G)	24 h	24 kPa	8 mm s^{-1}	0.25 mm	0.22 mm	130 ms	13%
	Cylindrical (25 G)	24 h	104 kPa	8 mm s^{-1}	0.25 mm	0.22 mm	130 ms	13%
GEL	Conical (25 G)	24 h	32 kPa	7 mm s^{-1}	0.25 mm	0.22 mm	130 ms	13%
	Cylindrical (25 G)	24 h	126 kPa	7 mm s^{-1}	0.25 mm	0.22 mm	130 ms	13%
ALG	Conical (25 G)	24 h	26 kPa	6 mm s^{-1}	0.25 mm	0.22 mm	130 ms	13%
	Cylindrical (25 G)	24 h	118 kPa	6 mm s^{-1}	0.25 mm	0.22 mm	130 ms	13%

extrusion process might impair the viscoelastic properties of bioinks. These tests highlight that, immediately after the printing, all the materials are subjected to a decrease of up to 25% of their original viscoelastic properties. In spite of this, the elastic modulus G' is still prevailing over the viscous one G'', indicating that solicitations experienced by the materials during the extrusion are not causing their transition from gel to sol-phase. Additionally, at this time-point the printed constructs seemed fragile, and it was almost impossible to handle them without damage, thus making impossible to safely place them in culture conditions. Tests carried out on constructs 45 min after their fabrication show that the original rheological characteristics were recovered, thus reiterating the self-healing behaviour of the Hep3Gel and control hydrogels (figure 7(b)). At this time-point the printed constructs were less delicate and could be handled more easily, without breaking.

However, since this delay could affect the fate of embedded cells, a post-processing curing step was then tuned by investigating the impact of $CaCl_2$ solutions at different concentrations, the aim was to compensate for such a temporary gap in terms of viscoelastic properties. Among the different concentrations of $CaCl_2$ considered, it was found that 0.1% (w/v) is successful in partially restoring, without overcrosslinking, the materials (figure 7(c)).

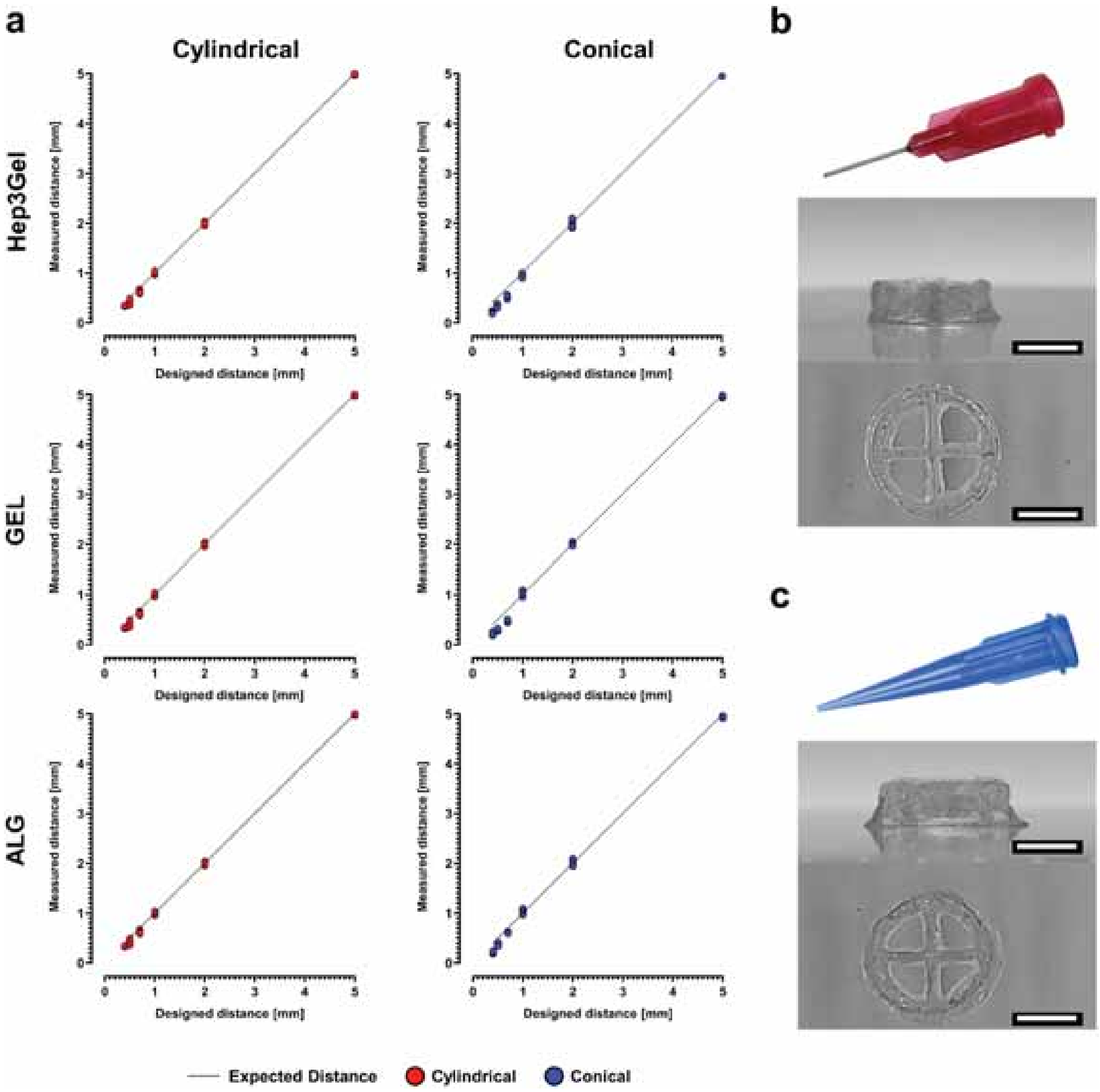

Figure 6. Resolution of the optimized printing process. (a) Measurements performed for Hep3Gel and control materials on the distances between contiguous fibres of a mono-layered serpentine with increasing curvature radius, providing for each material the resolution of the optimized printing process, both with cylindrical and conical nozzles. (b), (c) Orthogonal projections of the full-sized, 16-layered constructs printed with a cylindrical and a conical nozzle, respectively. Samples reported in (b) and (c) were both fabricated with Hep3Gel; the scale-bars correspond to 5.0 mm.

It was found that this process did not cause the shrinkage of printed constructs, whose shape remained stable for up to 12 d in culture conditions, with no significant differences related to the shape and dimension of porosity (figure S8).

3.6. Static culture of bioprinted constructs loaded with HepG2 cells

For the constructs fabricated with Hep3Gel, quantitative analyses of indicated a significant increase in viable cells. From day 6 cells starts to grow consistently, exceeding 200% of viability at day 12. This trend was not observed in the control materials, cell viability remained roughly constant through the whole experiment time course (figure 8(a)). These quantitative results are supported by CLSM observations (figures 8(b) and (c)). In the case of Hep3Gel, it was possible to qualitative observe an increase in green fluorescence intensity from the initial to the final time-point. This increase was not observed for the control materials. Finally, red fluorescence intensity was not seen to increase, in either the Hep3Gel or in control materials.

4. Discussion

Alginate is currently an extremely popular material for the production of bioinks, both for commercial and academic purposes. As such, it is both used as a standalone material and in combination with other materials, depending on each specific application [33, 34].

The most widespread contemporary approaches to the extrusion-based bioprinting of alginate-based constructs rely entirely on crosslinking processes which take place after extrusion, and through external

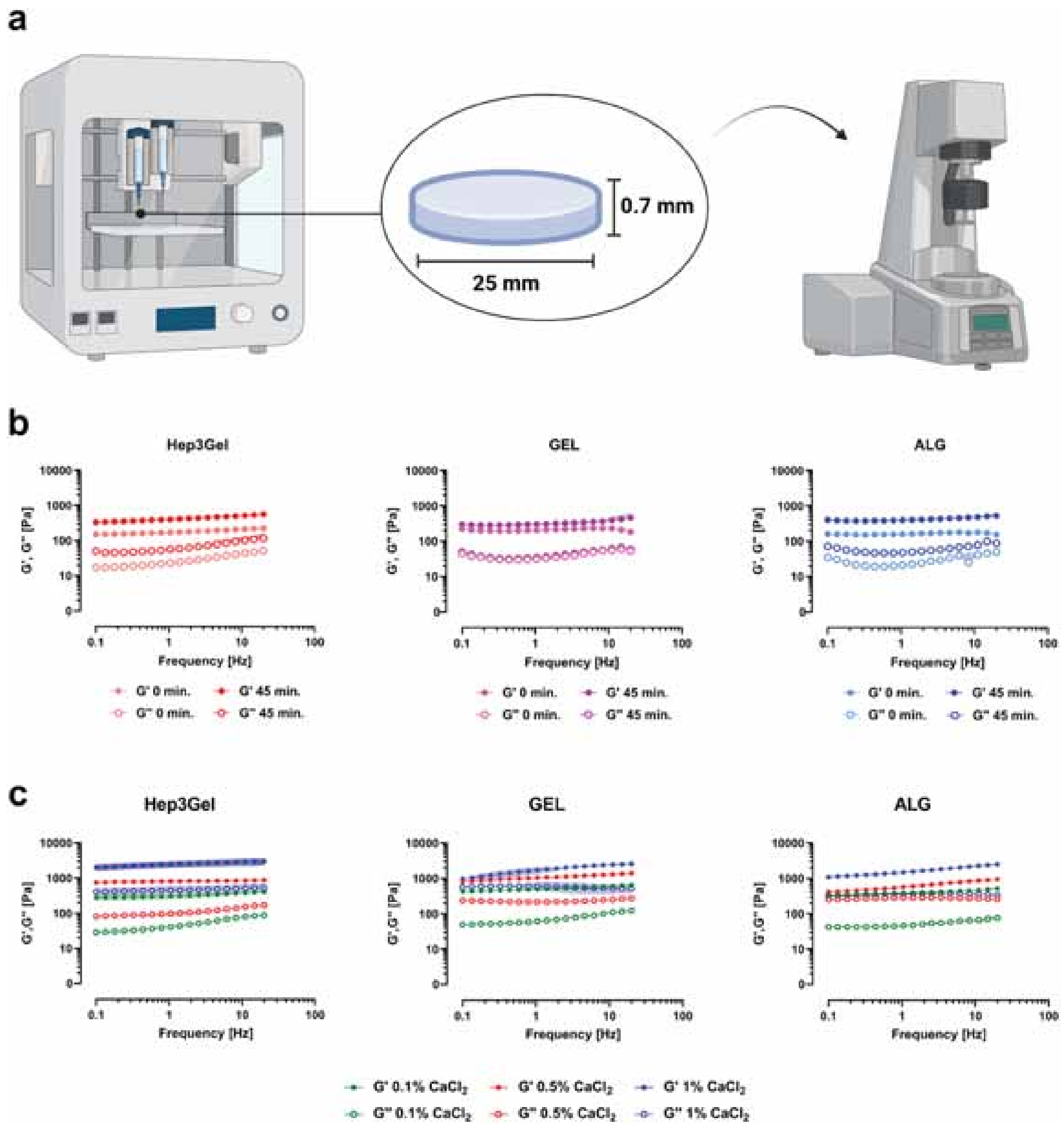

Figure 7. After-printing rheological behavior of the bioinks and possible post-processing. (a) Methodology followed to test printed samples; solid cylindric samples were printed with the studied bioinks and tested with the rheometer. The exploiting of solid geometries was necessary, since the macropores that were designed for cell-laden constructs might have impaired the analysis by creating gaps between rheometer plates. (b) Frequency-sweep tests show that Hep3Gel, GEL, and ALG temporarily lose their original viscoelastic properties after being printed. The original viscoelastic features are recovered after 45 min from the printing, highlighting the self-healing behaviour of the engineered inks. (c) Different options to post-process printed constructs through external gelation. Among them, it was found that exploiting a 0.1% (w/v) $CaCl_2$ solution in complete medium allows to recover the original properties, without over-crosslinking the materials.

gelation [35]. However, due to the nature of external gelation itself, this crosslinking method does not allow to fully control the viscoelastic properties of the printed construct and leads to the formation of gradients in terms of crosslinking degree, throughout the cross-section of the printed fibre, that can even culminate in the shrinkage of the printed structure. It was successfully demonstrated that alginate-based bioinks could be prevented from collapsing by reinforcing them through blends with other fillers (e.g. nanocellulose), thus overcoming this limitations [36]. In this context, internal gelation is not only useful to enable the full control over the viscoelastic properties of the inks, but also to reinforce the structure of the hydrogels, thus preventing them from shrinking. There do remain situations, though, in which the viscoelastic properties of the printed structure are a non-negligible requirement, as in cases where the fabricated constructs need to mimic a specific biomechanical environment [37–40]. In these cases, internal crosslinking represents an extremely potent tool, since it allows to both precisely control the viscoelastic properties of the bioink and to produce homogeneously crosslinked hydrogels [41, 42]. This is possible because divalent cations sources ($CaCO_3$) are already present within the pre-hydrogel alginate solutions, and homogeneously dispersed within them. However, since $CaCO_3$ is not soluble at physiological pH, Ca^{2+}

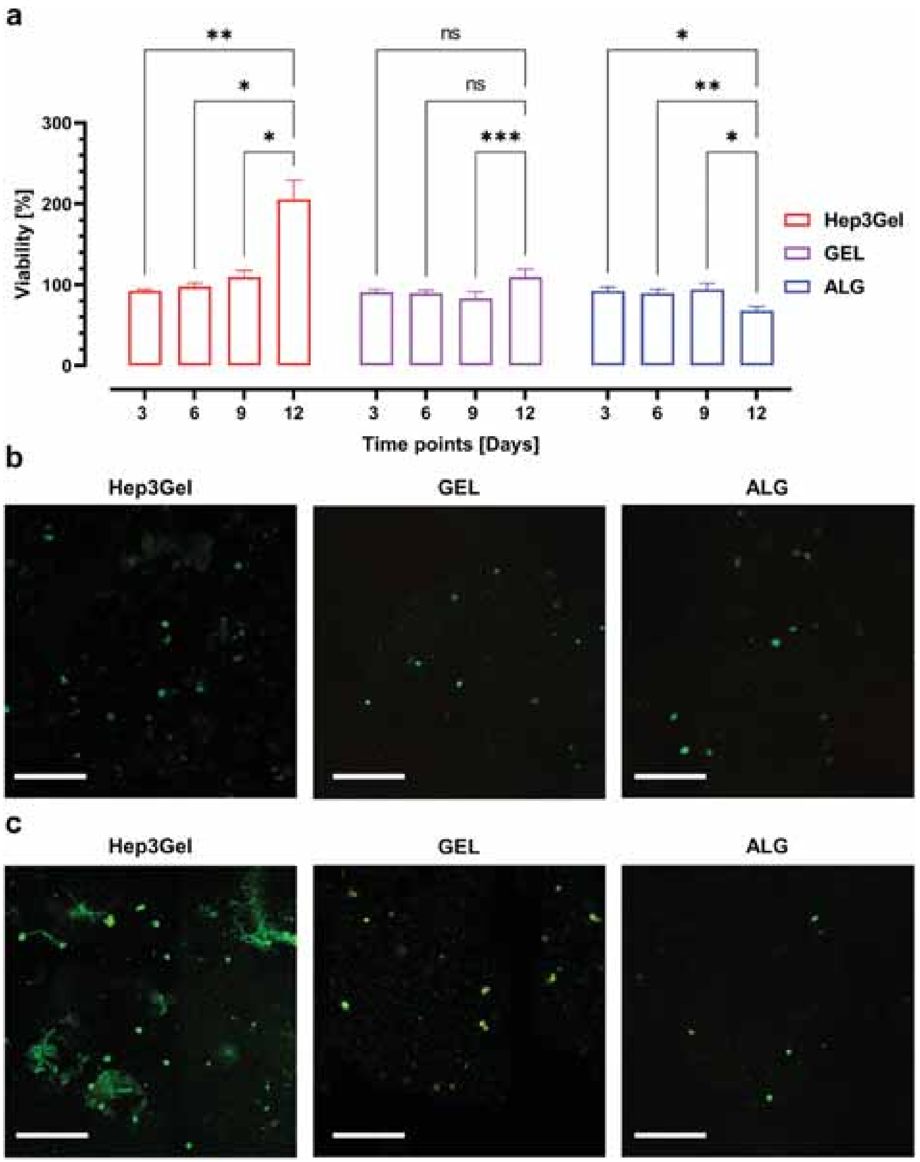

Figure 8. Viability analyses. (a) Quantitative data from Alamar Blue assay up to 12 d in culture. Data were normalized as a function of the viability after 4 h from the printing. (b) CLSM analyses with live/dead kit staining at day 0. (c) CLSM observation with live/dead kit on day 12. Scale bars correspond to 350 µm.

ions are not available for crosslinking alginate macromolecular chains. The dissolution of calcium carbonate, and the consequent release of crosslinking ions is triggered by the addition of GDL. The hydrolysis of this cyclic ester causes the progressive decrease of the pH, leading to the time-dependent dissolution of $CaCO_3$. This mechanism enables slow crosslinking kinetics, that allow the homogeneous gelation of the hydrogel throughout its volume [43, 44]. The dissolution of $CaCO_3$ also leads to the formation of CO_2 bubbles inside the cartridge. These can damage the macroscopic structure of the hydrogels, creating a multitude of breaking points that will negatively affect the printability of the hydrogel, as well as the fate of embedded cells [45]. This is why, once loaded with the bioinks, cartridges where not sealed with caps, but rather with 0.22 μm filters (as described in section 2.2.2), thus allowing the released CO_2 to vent, while maintaining the sterility inside the cartridge.

In addition to the fine control of viscoelastic properties, internal crosslinking is characterized by modulable crosslinking kinetics. This allows to precisely tailor the gelation rate. As regards the specific formulations of the materials described in this paper, the amount of GDL is directly related to the dissolution rate of $CaCO_3$ and so to the crosslinking speed [46, 47]. In particular, Hep3Gel was designed to be viable with extremely slow crosslinking kinetics, as previously discussed [20].

In the case of extrusion bioprinting, dealing with materials characterized by dynamic rheological properties represents a double-edged sword. The clear advantage of this approach is related to the flexibility.

In this sense, for as long as the crosslinking is progressing, it is like having a different available material at each time-point. Consequently, depending on the specific application, this allows to begin processing the ink at the exact moment in which it displays the optimal viscoelastic properties: an approach which is currently known as reactive bioprinting [21]. On the other hand, the presence of the time as an additional parameter to be considered during the optimization introduces significant complexity into the process, since each of the considered time-points are characterized by different properties and, as such, will require different optimal printing parameters to be found.

Aiming to narrow the focus, in this study the optimization of printability was run at the three time-points that coincide with significantly different values of the tanδ of Hep3Gel. This is because this parameter (that quantifies the solid/liquid-like behaviour of a hydrogel), together with the dimensional features of the crosslinking mesh, is known to be one of the main drivers that determine the printability of a material [48–50]. Additionally, the same analyses were performed at the end of the reaction, at the 24 h time-point and at this stage, the viscoelastic properties of all the hydrogel samples, as well as their *a priori* printability, were fully characterized in previous works [20].

The combination of results from the *a priori* study of printability showed that all the examined hydrogels are potentially suitable to be bioprinted at each of the considered time-points. They are not only able to flow through a cartridge in the presence of a determined shear stress, but are also able to recover their original viscoelastic properties after extrusion [51]. However, in the case of Hep3Gel at the 3 h time-point such recovery is slower and more progressive than when compared with the other samples we considered and as highlighted by the results from the shape-fidelity analysis, the fibres printed in this condition experienced unacceptably high levels of deformation, rendering them incapable of sustaining the printing of the designed geometry. This result was found to coincide with the value of tanδ being close to 1, indicating a more consistent contribution of the viscous component, that limited the elastic recovery of the printed fibres [21].

The feasibility of fabricating a specific structure does not only depend on the property of the employed inks, but also on the shape of the structure itself, thus highlighting the importance of *a priori* validating and defining the target geometry [20, 52]. Therefore, the optimization of printing parameters was not only performed through the quantitative analysis of shape-fidelity coefficients (that are measured on planar projections of the final geometry), but also through the further refinement was subsequently carried out on full sized structures. As specifically regards the computed shape-fidelity coefficients, the optimal value for each of them is represented by the unit value, with values smaller than 1 indicating a too-high degree of crosslinking in terms of the uniformity factor and a too-low degree of crosslinking in terms of the pore and the perimeter coefficients. Values greater than 1 indicate the opposite [19, 31]. These parameters can be further combined into the printability coefficient that reaches the unit value when perfectly straight fibres (with the same diameter as the one of the nozzle) are printed into geometries whose perimeters, and pore sizes and shapes, fit the CAD design [21]. In the specific case of this study, it is evident that the printability coefficient increases as a function of time, coming progressively closer to 1 and reaching its maximum at the 24 h time-point. It was also the case, for each bioink, that the best results were achieved when printing geometries at the minimal extrusion pressure, with a printhead speed that depends on the to-be-printed material.

Although this analysis provided useful insights to optimize the printability of the Hep3Gel and control materials we found that the situation can dramatically change when shifting from monolayered geometries to the printing of full-sized tri-dimensional constructs. In essence it was not possible to print the designed constructs with any of the samples due to structural collapses happening during the fabrication.

We hypothesized this to be caused by the balance between gravity and surface tensions. The action of gravity pushes down the constructs, causing fibres to flatten and in some cases even to merge, leading to shrinkage. On the other hand, the normal component of the surface tension acts in an opposite way to gravity, by pulling and drawing the constructs upwards [53, 54]. As a result, the successful printing of a self-standing construct can be achieved as long as the normal component of the surface tension prevails over the force of gravity, as shown in figure 9.

We postulated that this issue could be overcome by rebalancing the two forces. Since the surface tensions are dependent on the nature of the interfacing materials (substrate vs. bioink for the first layer, and bioink vs bioink for successive layers) the only way to modify this effect would have been to completely reformulate the inks [54, 55]. Our alternative approach, to avoid this scenario, was to use a thinner nozzle. In this way it was possible to print thinner and lighter fibres, thus reducing the gravity-related contribution, and allowing for the successful printing of the designed constructs.

When printing with the 25 G nozzles, in both cylindrical and conical configuration, it was found that the results from the shape-fidelity analysis for a 22 G nozzle could be translated and applied to the 25 G nozzles. We found that printing the geometries with 25 G nozzles at the 24 h time-point, using in each different case the minimal extrusion pressure together with the previously determined printhead speeds,

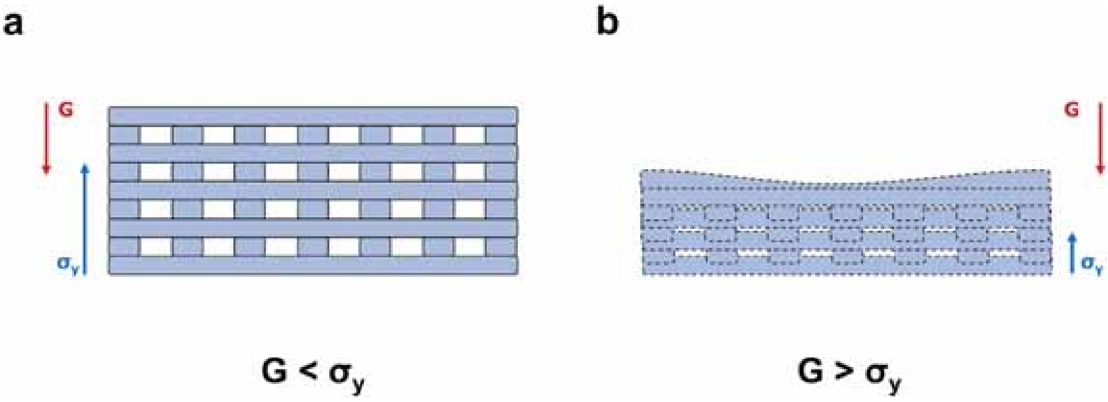

Figure 9. The balance between gravity and surface tensions, and its effect on 3D-printed structures. (a) The vertical component σ_y of the resulting of surface tensions acts oppositely to gravity and dominates over it. In these conditions, the printed construct can self-stand. (b) Conversely when gravity prevails over σ_y the printed fibres are flattened, causing the collapse of the printed geometry.

yielded quantitative results which were always close to the optimal values, with no statically significant differences between cylindrical and conical nozzles. We did, however, record a great degree of difference in terms of minimal extrusion pressure between cylindrical and conical configurations. This is consistent with recent findings in the field and is due to the higher stresses needed to extrude a bioink from a needle characterized by a constant diameter and as opposed to a conical shape, in which the final diameter is reached progressively. This can be explained by the fact that it is necessary to realign the chains of a hydrogel in order to make it flow through a nozzle. As a result of shape-factor, cylindrical nozzles provide a constant alignment of the mesh throughout their length and, as such, require higher pressures to enable the extrusion of the bioink than those needed when printing with a tapered nozzle of the same dimension [56, 57].

The higher degree of alignment provided by cylindrical nozzles leads to significantly lower resolutions when compared with conical ones [58]. However, the maximum level of detail needed to print the designed constructs is related to the characteristic dimensions of the four macropores, and it is roughly 1 order of magnitude greater than the resolution achievable by fabricating them with the conical nozzle. As a result, the printing of the designed structures is not negatively impacted by the worst resolution characterizing tapered nozzles. In light of these, and considering that cellular viability is directly impaired by the increase of the printing pressure, 25 G conical nozzles were chosen to print the cell-laden constructs with Hep3Gel and control materials [59, 60].

The apparent contradiction between the recovery of the viscoelastic properties forecasted by the *a priori* assessment of printability and the actual recovery times, recorded on printed constructs, is then a matter of particular interest. Although the causes underlying this contradiction remains unclear, we hypothesize that it could be due to different factors acting on the crosslinking mesh. Firstly, although the samples were subjected to oscillatory stresses and strains during the recovery test, the stresses experienced during the extrusion process are characterized by a different distribution and strains are expected to be higher [61]. These differences, in terms of the type and level of stresses acting on the inks when flowing through a tapered nozzle when compared with those which are typical of rheological measurement, may influence the behaviour of the ionic bonds between Ca^{2+} ions and the macromolecular chains of alginate which, in turn, would explain longer recovery times. Additionally, the fact that the characteristic dimension adopted during rheological analyses (the gap between plates) is 100% greater than that of the printing process (internal diameter of the nozzle) may also be significant. Finally, the distortion and orientation of the network of alginate polymeric chains which occurs during the extrusion cannot be mimicked through rheological tests and could also be responsible for the transitory loss, followed by the progressive recovery, of viscoelastic properties. In the end, despite the inaccuracy of predicted recovery times, the *a priori* analysis was found to be a useful tool to investigate the ability of the hydrogels to recover their original properties, as this is a major aspect to be considered when engineering a bioink [62–64].

The post-processing of printed constructs with $CaCl_2$ was thus tuned aiming to provide the immediate reinforcement on the external layer of the structures. This allowed them to be handled without breakage and placed in culture conditions as quickly as possible, limiting the time of cells outside the incubator environment. In this way, a double crosslinking strategy was exploited to print internally crosslinked alginate-based hydrogels that were subsequently cured through external gelation. To date, a similar procedure has already been described by using internal gelation as a pre-crosslinking technique to increase the viscosity of alginate-based bioinks in order to reduce the relaxation of printed fibres, then printed constructs are fixed with external crosslinking with $CaCl_2$ solutions [19, 65].

Although there are procedural similarities between these and our approach, there are substantive and significant differences. In our approach, with Hep3Gel, internal gelation has been developed as the dominant crosslinking mechanism (rather than as a pre-crosslinking). It enabled at the same time to fully control the viscoelastic properties of the to-be-printed structures, as well as to provide the structural stability of the printed scaffolds, thus allowing per se to overcome the two main limitations that are traditionally connected to the use of alginate bioinks [19, 36, 66].

Conversely, in our case, external gelation was used only to stabilize the constructs. Aiming to place cultured cells as soon as possible within a favourable environment, while the original crosslinking mesh in the internal regions of the structure is fully reconstructed, thus providing the constructs with the originally designed viscoelastic properties.

Our fabrication approach is suitable for sustaining the growth of embedded HepG2 cells for up to 12 d. The enhanced cellular growth which can be observed by comparing Hep3Gel with the control materials is consistent with previous findings on the beneficial effects of the extracellular matrix powder compounds on cellular growth [67–69]. However, in previous studies carried out on homogeneous constructs produced with Hep3Gel, it was not possible to extend the culture above day 8, due to the progressive and unstoppable decay in terms of cell viability after this time-point [20]. These results obtained in static cultures are extremely promising, and lay the foundations to successfully shift to dynamic culture strategies.

It is for this reason that the adoption of extrusion-based bioprinting represents a game-changing approach. The extension of the culture time can only be explained by the presence of macropores that maximize the exchange surfaces. This improvement allows for homogeneous degrees of oxygenation but also promotes the exchange of nutrients, even in the core regions of the constructs, as forecasted by *a priori* computational simulations. In this sense, the fabrication of macroporous structures allows us to mimic a key feature of the hepatic tissue, one of the five most perfused and oxygenated organs of the human body [70–72]. At this point, we believe that further studies should be focused on the assessment of the metabolic functionality of embedded cells, which is a crucial requirement to effectively model hepatic tissue [4]. This could be supported by further exploration of the culture of cell types that are more metabolically relevant than HepG2, such as primary hepatocytes, iPSC-derived hepatocytes, or HepaRG cells [73–75].

5. Conclusions

Internal gelation is a powerful approach that allows to overcome the two main issues characterizing the extrusion-based bioprinting of alginate-based bioinks. Firstly, the final viscoelastic properties of the printed scaffold are fully controlled, and can be finely tuned, also avoiding the undesired and uncontrolled formation of crosslinking gradients. Additionally, this approach enables the fabrication of self-standing structures, without needing to blend alginate with other materials that can improve the structural integrity of the construct, neither requiring to extrude the bioink within crsosslinking baths or supporting sacrificial hydrogels. In this work, we have presented a straightforward methodology for the optimization of the printability for this type of bioinks. In the context of this specific study, it was demonstrated that Hep3Gel and the control materials are not suitable for reactive bioprinting. This is not to say, that this approach may not prove to be useful with other to-be-printed geometries.

The methodology presented was suitable to optimize the printing parameters for the fabrication of the designed constructs, allowing for the printing of 14-layered self-standing structures which are characterized by the maintenance of the predetermined final viscoelastic properties. Due to the solicitations typical of the extrusion process, a curing step through external gelation is necessary to stabilize the constructs, especially in case where the minimization of the time out of the incubator is a primary requirement.

The adoption of a macroporous 3D-bioprinted geometry leads to higher and homogeneous oxygenation levels, even in the core regions of the constructs. This has allowed us to extend the culture time by up to 50% when compared with studies carried out on homogeneous hydrogels. Additionally, the presence of ECM powder positively impacted the fate of embedded cells, leading to the enhancement of cellular viability during the experimental course. As a result, further studies should be focused on adopting this process to fabricate and culture constructs that embed more metabolically relevant cell types. This may allow for the complete validation of the model proposed in this paper.

Data availability statement

The data cannot be made publicly available upon publication because the cost of preparing, depositing and hosting the data would be prohibitive within the terms of this research project. The data that support the findings of this study are available upon reasonable request from the authors.

Acknowledgments

This research project was funded by the Italian Ministry of Health (Prot. n. 0025345 del 04/12/2020), and by a Grant of the Italian Ministry of Education, University and Research (MIUR) to the Department of Molecular Medicine of the University of Pavia under the initiative 'Dipartimenti di Eccellenza (2023–2027)'. We are grateful to P Vaghi (Centro Grandi Strumenti, Confocal Microscopy https://cgs.unipv.it/eng/, University of Pavia, Pavia, Italy) for the technical assistance in the CLSM studies. A special thanks to S Burgess (University of Pavia) for revising the English of the manuscript.

Authorship contribution statement

Conceptualization: P Petrini, L Visai, G Guagliano. Methodology: P Petrini, F Briatico-Vangosa, L Visai, F Donnaloja, G Guagliano. Formal analysis: G Guagliano. Investigation: G Guagliano, C Volpini, F Donnaloja, J Camilletti. Writing—Original Draft: G Guagliano. Writing—Review & Editing: all the authors contributed equally. Visualization: G Guagliano. Supervision: P Petrini, L Visai, F Briatico-Vangosa. Funding acquisition: P Petrini, L Visai, F Briatico-Vangosa.

Conflict of interest

The authors declare no competing interests.

ORCID iDs

Giuseppe Guagliano https://orcid.org/0000-0003-1059-1505
Cristina Volpini https://orcid.org/0000-0003-4483-2776
Jacopo Camilletti https://orcid.org/0000-0002-4113-2101
Francesca Donnaloja https://orcid.org/0000-0001-9927-309X
Francesco Briatico-Vangosa https://orcid.org/0000-0002-7088-1064
Livia Visai https://orcid.org/0000-0003-1181-3632
Paola Petrini https://orcid.org/0000-0002-5081-5254

References

[1] Choi Y J, Park H, Ha D H, Yun H S, Yi H G and Lee H 2021 3D bioprinting of *in vitro* models using hydrogel-based bioinks *Polymer* **13** 366
[2] Chen Y *et al* 2020 Noninvasive *in vivo* 3D bioprinting *Sci. Adv.* **6**
[3] Hong N, Yang G H, Lee J H and Kim G H 2018 3D bioprinting and its *in vivo* applications *J. Biomed. Mater. Res.* B **106** 444–59
[4] Guagliano G, Volpini C, Briatico-Vangosa F, Cornaglia A I, Visai L and Petrini P 2022 Toward 3D-bioprinted models of the liver to boost drug development *Macromol. Biosci.* **22** 2200264
[5] Ramiah P, du Toit L C, Choonara Y E, Kondiah P P D and Pillay V 2020 Hydrogel-based bioinks for 3D bioprinting in tissue regeneration *Front. Mater.* **7** 76
[6] Hospodiuk M, Dey M, Sosnoski D and Ozbolat I T 2017 The bioink: a comprehensive review on bioprintable materials *Biotechnol. Adv.* **35** 217–39
[7] Ma Y *et al* 2018 3D spatiotemporal mechanical microenvironment: a hydrogel-based platform for guiding stem cell fate *Adv. Mater.* **30** 1705911
[8] Ma Y *et al* 2021 Viscoelastic cell microenvironment: hydrogel-based strategy for recapitulating dynamic ECM mechanics *Adv. Funct. Mater.* **31** 2100848
[9] Tappa K and Jammalamadaka U 2018 Novel biomaterials used in medical 3D printing techniques *J. Funct. Biomater.* **9** 17
[10] Vanaei S, Parizi M S, Salemizadehparizi F and Vanaei H R 2021 An overview on materials and techniques in 3D bioprinting toward biomedical application *Eng. Regen.* **2** 1–18
[11] Axpe E and Oyen M L 2016 Applications of alginate-based bioinks in 3D bioprinting *Int. J. Mol. Sci.* **17** 1976
[12] Chan L W, Lee H Y and Heng P W S 2006 Mechanisms of external and internal gelation and their impact on the functions of alginate as a coat and delivery system *Carbohydrate Polym.* **63** 176–87
[13] Shah P P, Shah H B, Maniar K K and Özel T 2020 Extrusion-based 3D bioprinting of alginate-based tissue constructs *Procedia CIRP* **95** 143–8
[14] Jia J *et al* 2014 Engineering alginate as bioink for bioprinting *Acta Biomater.* **10** 4323–31
[15] Rastogi P and Kandasubramanian B 2019 Review of alginate-based hydrogel bioprinting for application in tissue engineering *Biofabrication* **11** 042001
[16] Shapira A, Noor N, Asulin M and Dvir T 2018 Stabilization strategies in extrusion-based 3D bioprinting for tissue engineering *Appl. Phys. Rev.* **5** 041112
[17] Ghanizadeh Tabriz A, Hermida M A, Leslie N R and Shu W 2015 Three-dimensional bioprinting of complex cell laden alginate hydrogel structures *Biofabrication* **7** 045012
[18] Corbett D C, Olszewski E and Stevens K 2019 A FRESH take on resolution in 3D bioprinting *Trends Biotechnol.* **37** 1153–5
[19] Hazur J, Detsch R, Karakaya E, Kaschta J, Teßmar J, Schneidereit D, Friedrich O, Schubert D W and Boccaccini A R 2020 Improving alginate printability for biofabrication: establishment of a universal and homogeneous pre-crosslinking technique *Biofabrication* **12** 045004
[20] Guagliano G, Volpini C, Sardelli L, Bloise N, Briatico-Vangosa F, Cornaglia A I, Dotti S, Villa R, Visai L and Petrini P 2023 Hep3Gel: a shape-shifting extracellular matrix-based, three-dimensional liver model adaptable to different culture systems *ACS Biomater. Sci. Eng.* **9** 211–29
[21] Sardelli L, Tunesi M, Briatico-Vangosa F and Petrini P 2021 3D-reactive printing of engineered alginate inks *Soft Matter* **17** 8105–17
[22] Ma Y, Ji Y, Huang G, Ling K, Zhang X and Xu F 2015 Bioprinting 3D cell-laden hydrogel microarray for screening human periodontal ligament stem cell response to extracellular matrix *Biofabrication* **7** 044105
[23] Ma Y, Ji Y, Zhong T, Wan W, Yang Q, Li A, Zhang X and Lin M 2017 Bioprinting-based PDLSC-ECM screening for *in vivo* repair of alveolar bone defect using cell-laden, injectable and photocrosslinkable hydrogels *ACS Biomater. Sci. Eng.* **3** 3534–45
[24] Singh G and Chanda A 2021 Mechanical properties of whole-body soft human tissues: a review *Biomed. Mater.* **16** 062004

[25] Tunesi M, Izzo L, Raimondi I, Albani D and Giordano C 2020 A miniaturized hydrogel-based *in vitro* model for dynamic culturing of human cells overexpressing beta-amyloid precursor protein *J. Tissue Eng.* **11** 1–17

[26] Pacheco D P, Butnarasu C S, Briatico Vangosa F, Pastorino L, Visai L, Visentin S and Petrini P 2019 Disassembling the complexity of mucus barriers to develop a fast screening tool for early drug discovery *J. Mater. Chem.* B **7** 4940–52

[27] Turco G, Donati I, Grassi M, Marchioli G, Lapasin R and Paoletti S 2011 Mechanical spectroscopy and relaxometry on alginate hydrogels: a comparative analysis for structural characterization and network mesh size determination *Biomacromolecules* **12** 1272–82

[28] Bonfanti A, Kaplan J L, Charras G and Kabla A 2020 Fractional viscoelastic models for power-law materials *Soft Matter* **16** 6002–20

[29] Grassi M, Farra R, Fiorentino S M, Grassi G and Dapas B 2015 Hydrogel Mesh Size Evaluation *Polysaccharide Hydrogels: Characterization and Biomedical Applications* 1st edn, ed P Matricardi, F Alhaique and T Coviello (New York: Jenny Stanford Publishing) (https://doi.org/10.1201/b19751)

[30] Schindelin J *et al* 2012 Fiji: an open-source platform for biological-image analysis *Nat. Methods* **9** 676–82

[31] Ouyang L, Yao R, Zhao Y and Sun W 2016 Effect of bioink properties on printability and cell viability for 3D bioplotting of embryonic stem cells *Biofabrication* **8** 035020

[32] Eilenberger C, Kratz S R A, Rothbauer M, Ehmoser E K, Ertl P and Küpcü S 2018 Optimized alamarBlue assay protocol for drug dose-response determination of 3D tumor spheroids *MethodsX* **5** 781–7

[33] Shams E, Barzad M S, Mohamadnia S, Tavakoli O and Mehrdadfar A 2022 A review on alginate-based bioinks, combination with other natural biomaterials and characteristics *J. Biomater. Appl.* **37** 355–72

[34] Leonardo M, Prajatelistia E and Judawisastra H 2022 Alginate-based bioink for organoid 3D bioprinting: a review *Bioprinting* **28** e00246

[35] Piras C C and Smith D K 2020 Multicomponent polysaccharide alginate-based bioinks *J. Mater. Chem.* B **8** 8171–88

[36] Markstedt K, Mantas A, Tournier I, Martínez Ávila H, Hägg D and Gatenholm P 2015 3D bioprinting human chondrocytes with nanocellulose-alginate bioink for cartilage tissue engineering applications *Biomacromolecules* **16** 1489–96

[37] Ye S, Boeter J W B, Penning L C, Spee B and Schneeberger K 2019 Hydrogels for liver tissue engineering *Bioengineering* **6** 59

[38] Li X, Sun Q, Li Q, Kawazoe N and Chen G 2018 Functional hydrogels with tunable structures and properties for tissue engineering applications *Front. Chem.* **6** 499

[39] Tejo-Otero A, Fenollosa-Artés F, Achaerandio I, Rey-Vinolas S, Buj-Corral I, Mateos-Timoneda M Á and Engel E 2022 Soft-tissue-mimicking using hydrogels for the development of phantoms *Gels* **8** 40

[40] Pacheco D P, Vargas N S, Visentin S and Petrini P 2021 From tissue engineering to engineering tissues: the role and application of *in vitro* models *Biomater. Sci.* **9** 70

[41] Quong D, Neufeld R J, Skjåk-Braek G and Poncelet D 1998 External versus internal source of calcium during the gelation of alginate beads for DNA encapsulation *Inc. Biotechnol. Bioeng.* **57** 438–46

[42] Moreira H R, Munarin F, Gentilini R, Visai L, Granja P L, Tanzi M C and Petrini P 2014 Injectable pectin hydrogels produced by internal gelation: pH dependence of gelling and rheological properties *Carbohydrate Polym.* **103** 339–47

[43] Cardoso A Z, Alvarez Alvarez A E, Cattoz B N, Griffiths P C, King S M, Frith W J and Adams D J 2014 The influence of the kinetics of self-assembly on the properties of dipeptide hydrogels *Faraday Discuss.* **166** 101–16

[44] Paques J P 2015 Alginate nanospheres prepared by internal or external gelation with nanoparticles *Microencapsul. Microspheres Food Applications* (Amsterdam: Academic) pp 39–55

[45] Walls P L L, McRae O, Natarajan V, Johnson C, Antoniou C and Bird J C 2017 Quantifying the potential for bursting bubbles to damage suspended cells *Sci. Rep.* **7** 1–9

[46] Growney Kalaf E A, Flores R, Bledsoe J G and Sell S A 2016 Characterization of slow-gelling alginate hydrogels for intervertebral disc tissue-engineering applications *Mater. Sci. Eng.* C **63** 198–210

[47] Liu G, Zhou H, Wu H, Chen R and Guo S 2016 Preparation of alginate hydrogels through solution extrusion and the release behavior of different drugs *J. Biomater. Sci. Polym. Ed.* **27** 1808–23

[48] Gao T, Gillispie G J, Copus J S, Asari A K P R, Seol Y-J, Atala A, Yoo J J and Lee S J 2018 Optimization of gelatin-alginate composite bioink printability using rheological parameters: a systematic approach *Biofabrication* **10** 034106

[49] Malekpour A and Chen X 2022 Printability and cell viability in extrusion-based bioprinting from experimental, computational, and machine learning views *J. Funct. Biomater.* **13** 40

[50] Naghieh S and Chen X 2021 Printability–A key issue in extrusion-based bioprinting *J. Pharm. Anal.* **11** 564–79

[51] Paxton N, Smolan W, Böck T, Melchels F, Groll J and Jungst T 2017 Proposal to assess printability of bioinks for extrusion-based bioprinting and evaluation of rheological properties governing bioprintability *Biofabrication* **9** 044107

[52] Bonatti A F, Chiesa I, Vozzi G and De Maria C 2021 Open-source CAD-CAM simulator of the extrusion-based bioprinting process *Bioprinting* **24** e00172

[53] Ribeiro A, Blokzijl M M, Levato R, Visser C W, Castilho M, Hennink W E, Vermonden T and Malda J 2017 Assessing bioink shape fidelity to aid material development in 3D bioprinting *Biofabrication* **10** 014102

[54] Xu X, Jagota A, Peng S, Luo D, Wu M and Hui C-Y 2013 Gravity and surface tension effects on the shape change of soft materials *Langmuir* **29** 8665–74

[55] Piskunov M, Semyonova A, Khomutov N, Ashikhmin A and Yanovsky V 2021 Effect of rheology and interfacial tension on spreading of emulsion drops impacting a solid surface *Phys. Fluids* **33** 1–15

[56] Magalhães I P, de Oliveira P M, Dernowsek J, Casas E B L and Casas M S L 2019 Investigation of the effect of nozzle design on rheological bioprinting properties using computational fluid dynamics *Matéria* **24**

[57] Reina-Romo E, Mandal S, Amorim P, Bloemen V, Ferraris E and Geris L 2021 Towards the experimentally-informed in silico nozzle design optimization for extrusion-based bioprinting of shear-thinning hydrogels *Front. Bioeng. Biotechnol.* **9** 694

[58] Lee J M, Ng W L and Yeong W Y 2019 Resolution and shape in bioprinting: strategizing towards complex tissue and organ printing *Appl. Phys. Rev.* **6** 011307

[59] Fakhruddin K, Anwar Hamzah M S and Abd Razak S I 2018 Effects of extrusion pressure and printing speed of 3D bioprinted construct on the fibroblast cells viability *IOP Conf. Ser.: Mater. Sci. Eng.* **440** 012042

[60] Nair K, Gandhi M, Khalil S, Yan K C, Marcolongo M, Barbee K and Sun W 2009 Characterization of cell viability during bioprinting processes *Biotechnol. J.* **4** 1168–77

[61] Boularaoui S, Al Hussein G, Khan K A, Christoforou N and Stefanini C 2020 An overview of extrusion-based bioprinting with a focus on induced shear stress and its effect on cell viability *Bioprinting* **20** e00093

[62] Chopin-Doroteo M, Mandujano-Tinoco E A and Krötzsch E 2021 Tailoring of the rheological properties of bioinks to improve bioprinting and bioassembly for tissue replacement *Biochim. Biophys. Acta-Gen. Subj.* **1865** 129782

[63] Hölzl K, Lin S, Tytgat L, van Vlierberghe S, Gu L and Ovsianikov A 2016 Bioink properties before, during and after 3D bioprinting *Biofabrication* **8** 032002

[64] Ouyang L 2022 Pushing the rheological and mechanical boundaries of extrusion-based 3D bioprinting *Trends Biotechnol.* **40** 891–902

[65] Liu S *et al* 2019 Bioactive and biocompatible macroporous scaffolds with tunable performances prepared based on 3D printing of the pre-crosslinked sodium alginate/hydroxyapatite hydrogel ink *Macromol. Mater. Eng.* **304** 1800698

[66] Freeman F E and Kelly D J 2017 Tuning alginate bioink stiffness and composition for controlled growth factor delivery and to spatially direct MSC fate within bioprinted tissues *Sci. Rep.* **7** 1–12

[67] Lee H J, Mun S, Pham D M and Kim P 2021 Extracellular matrix-based hydrogels to tailoring tumor organoids *ACS Biomater. Sci. Eng.* **7** 4128–35

[68] Abbott A and Coburn J M 2021 HepaRG maturation in silk fibroin scaffolds: toward developing a 3D *in vitro* liver model *ACS Biomater. Sci. Eng.* (https://doi.org/10.1021/acsbiomaterials.0c01584)

[69] Giobbe G G *et al* 2019 Extracellular matrix hydrogel derived from decellularized tissues enables endodermal organoid culture *Nat. Commun.* **10** 1–14

[70] Pittman R N 2011 *Regulation of Tissue Oxygenation* 2nd edn, ed D N Granger and J P Granger (San Rafael, CA: Morgan & Claypool Life Sciences) (https://doi.org/10.4199/C00140ED2V01Y201606ISP065)

[71] Eipel C, Abshagen K and Vollmar B 2010 Regulation of hepatic blood flow: the hepatic arterial buffer response revisited *World J. Gastroenterol.* **16** 6046–57

[72] Li W, Li P, Li N, Du Y, S L, Elad D and Long M 2021 Matrix stiffness and shear stresses modulate hepatocyte functions in a fibrotic liver sinusoidal model *Am. J. Physiol.* **320** G272–82

[73] Akram M, Iquebal M, Naimuddin K, Sahi J, Grepper S and Smith C 2016 Hepatocytes as a tool in drug metabolism, transport and safety evaluations in drug discovery *Curr. Drug Discov. Technol.* **7** 188–98

[74] Corbett J L and Duncan S A 2019 iPSC-derived hepatocytes as a platform for disease modeling and drug discovery *Front. Med.* **6** 265

[75] Lübberstedt M, Müller-Vieira U, Mayer M, Biemel K M, Knöspel F, Knobeloch D, Nüssler A K, Gerlach J C and Zeilinger K 2011 HepaRG human hepatic cell line utility as a surrogate for primary human hepatocytes in drug metabolism assessment *in vitro J. Pharmacol. Toxicol. Methods* **63** 59–68